Compression and deposition of microgel monolayers from fluid interfaces: particle size effects on interface microstructure and nanolithography[†]

Laura Scheidegger,[a] **Miguel Ángel Fernández-Rodríguez,**[a] **Karen Geisel,** [b] **Michele Zanini,**[a] **Roey Elnathan,**[c] **Walter Richtering,** [b] **and Lucio Isa**[a∗]

Controlling the microstructure of monolayers of microgels confined at a water/oil interface is the key to their successful application as nanolithography masks after deposition on a solid substrate. Previous work demonstrated that compression of the monolayer can be used to tune the microgel arrangement and to explore the full two-dimensional area-pressure phase diagram of the particles trapped at the interface. Here, we extend these studies to two microgels of significantly different sizes, with 200nm and 1.5μm bulk diameters, resepectively. We start by investigating the properties of isolated particles in-situ at the interface by freeze-fracture cryo-SEM, and after deposition using an atomic force microscope. We then study their collective behavior in a compressed monolayer and highlight significant differences in terms of the accessible phases and their transitions. More specifically, the larger microgels behave similarly to colloids with a hard core and a soft polymeric shell, exhibiting capillarity-driven clustering at large specific area and a solid-solid phase transition between two hexagonal lattices at higher compressions. The smaller particles instead show no capillary forces and a smooth transition from an hexagonal lattice to a dense disordered monolayer. Finally, we demonstrate that the larger microgels can be effectively turned into masks for the fabrication of vertically aligned silicon nanowires by means of metal-assisted chemical etching. These findings highlight the subtle interplay between particle architecture, adsorption and interactions at the interface, whose understating and harnessing are at the basis of their successful use as nanopatterning tools.

1 Introduction

Colloidal monolayers are often employed to produce two-dimensional patterns on solid substrates[1]. The advantages of using micro or nanoparticles for patterning lie in the parallel nature of the process, i.e. allowing coating large areas in a single step, and in the degree of tuneability of the features' size and of their spatial arrangement. The former characteristic is generally dictated by the particle size, where each colloid typically corresponds to a single patterned feature, while the latter one is determined by the the interactions among the particles and with the substrate, which define the microstructure of the monolayer. A particularly interesting class of particles for 2D patterning are microgels.

Microgels are colloidal particles consisting of highly swollen cross-linked polymer networks, which can be synthesized over a large range of sizes and from a variety of different polymers[2]. Among the most widely studied microgels there are poly(N-isopropylacrylamide) (pNipam) particles. These

† Electronic Supplementary Information (ESI) available: [details of any supplementary information available should be included here]. See DOI: 10.1039/b000000x/

a Laboratory for Interfaces, Soft matter and Assembly, Department of Materials, ETH Zurich, Vladimir-Prelog-Weg 5, 8093 Zurich, Switzerland; E-mail: lucio.isa@mat.ethz.ch

b Institute of Physical Chemistry, RWTH Aachen University, Landoltweg 2, 52056 Aachen, Germany.

c ARC Centre of Excellence in Convergent Bio-Nano Science and Technology, Future Industries Institute, University of South Australia, Mawson Lakes, 5095, Australia.

particles are in a swollen (hydrated) state below 32 °C and in a partly collapsed (dehydrated) state above 32 °C, which is their so called volume-phase-transition temperature. The responsiveness of different microgels to external stimuli such as temperature, pH and ionic strength can be exploited in fundamental studies[3] and for many applications, including enhanced oil recovery, biomaterials, nanoreactions, drug delivery, chemical sensing and catalysis[2,4]. The softness of the particles, combined to the tuneability of their interactions, renders them also very promising candidates to obtain monolayers of controlled microstructure. Monolayers of microgels have for instance been used to fabricate microlens arrays[5,6] and interferometers[7], to obtain structural colors on solid supports[8], as well as substrates for cell culture[9], to form films[10] and for surface patterning[11–14]. Additionally, inorganic particles can also be embedded in microgel shells, where the soft hydrogel can be used to template the arrangement of the functional cores[15–21]. Most often, microgels synthesized in a one-pot reaction, where the polymerization and the cross-linking happen simultaneously, end up displaying a gradient of cross-linking density across their diameter[22,23]. As a consequence of this, the particles exhibit a core-shell morphology, which strongly affects their interactions and thus the monolayer microstructure. Finally, microgels can be highly surface-active and can therefore readily adsorb and assemble into monolayers at water-air or water-oil interfaces due to electrostatic and steric

interactions[24,25]. These interfacial monolayers can be further transferred to a solid substrate, as previously shown[26]. In particular, the combination of the core-shell morphology and their ability to self-assemble at interfaces can be used to provide fine tuning and control of the system, as particle monolayers are compressed to form richly varied two-dimensional structures, e.g. in a Langmuir trough. This concept has been used in previous studies for pNipam and P(Nipam-co-MAA) (MAA = methacrylic acid) core-shell microgels[27,28]. Depending on the surface pressure, the microgels acquire different arrangements, starting from an expanded fluid phase to a hexagonal close-packed lattice. In the close-packed lattice, the cores of the microgels are in contact[28]. Between the fluid and the close-packed states, there is an intermediate, non-close-packed hexagonal phase, where the shells of the microgels are in steric contact. By simultaneously compressing the barriers of the Langmuir trough and lifting a substrate through the interface, all these states can be transferred onto the substrate[26].

These monolayers have been deposited and used to lithographically fabricate arrays of vertically aligned silicon nanowires (VA-SiNWs) by wet-etching[14,29,30]. VA-SiNWs are used in many different fields and applications, as in batteries[31–34], in photonics[35], for bacterial recognition[36], cell transfection[30], and for anti-reflective surfaces[37], and electronics[38]. Various fabrication methods are used to create VA-SiNW. In addition to wet-etching methods[35], lithographic techniques in combination with etching[32,37,39,40] and growth routes, like vapor-liquid-solid growth[38,41], have been proposed. However, many of these processes have major drawbacks, including high cost, limited control over length, diameter, location and crystallographic orientation of the nanowires, and low throughputs. Thus, it is desired to have a precise and reliable fabrication method which is scalable and cheap. To this end, a new fabrication route named soft nanoparticle templating was developed[14]. In this technique, microgels are spread at a water/oil interface in a Langmuir trough. Then, they are compressed while simultaneously a silicon substrate is lifted through the water/oil interface for transfer. If the particles are in the non-close-packed hexagonal phase, their spacing can be precisely controlled over a range of several hundred nanometers[14] and these microgel arrays can later be swollen in photoresist and employed as etching masks to produce VA-SiNWs with high control over diameter, spacing and length using metal-assisted chemical etching (MACE)[14,29–31,33,39,40].

In spite of the promising results for the fabrication of SiNWs, open questions remain on whether the same strategy can be extended to microgels of different sizes and on how particle size and architecture affect the interface microstructure. Answering this questions would establish if this approach could be applied to a larger range of interparticle spacings and particle diameters for soft-colloidal templates. We therefore here study the interfacial adsorption, assembly, com-

pression and deposition of core-shell microgels with bulk sizes of $1.45\,\mu m$ and $214\,nm$, respectively significantly larger and smaller than previously studied particles. We furthermore investigate whether these particles can be effectively used as masks to produce VA-SiNWs obtained by MACE and if their size can be additionally tuned by O_2 plasma.

2 Results and Discussion

2.1 Morphology of microgels at water/oil interfaces and after deposition

Before moving into the details of the microstructure of interfacial microgel monolayers under compression, it is worth briefly discussing the properties of single microgel particles, both in bulk and at the interface. In this work we use two differently sized microgels out of the same material, p(Nipam-co-MAA), but the largest one of them has an additional pure pNipam outer shell. In bulk aqueous suspensions, these particles are sphere-like objects, exhibiting both temperature and pH responsiveness. In particular, they are highly swollen below their volume-phase-transition temperature of 32 °C and partially collapse at higher temperatures[2,4]. They also change their degree of swelling as a function of pH, being less swollen in acidic conditions than they are in basic conditions[27,28,42,43]. In this work, we do not make use of their responsiveness to environmental stimuli and we focus on the simplest case of them being dispersed in Milli-Q water. The two different particles studied in this work have the following hydrodynamic diameters of $(1454 \pm 278)\,nm$ and $(214 \pm 1)\,nm$ as measured by DLS in Milli-Q water, respectively larger and smaller than similar microgels we used for previous studies, which provide a useful reference[14,26]. The particles are termed Big and Small from here on. More details on the microgels and their synthesis are given in section 3.0.1.

As previously introduced, microgels obtained in a one-pot synthetic process typically display a core-shell morphology, with more densely cross-linked cores and shells of loosely cross-linked or dangling polymer chains. The core-shell nature of the particles becomes even more pronounced when they are adsorbed at an oil-water interface. In this case, the microgels are fully hydrated on the water side and poorly solvated in oil, and at the same time they show a high interfacial activity, implying a strong drive for the polymer to be localized at the interface. The combination of there factors leads to a deformation and stretching of the particles as they adsorb, accompanied by a very limited protrusion into the oil phase. The extent by which the particles deform and protrude depends on their chemical composition and cross-linking density[42] and on the chemical nature of the two fluid phases.

In order to investigate the morphologies of our particles at water-decane interfaces we employed freeze-fracture shadow-casting cryo-SEM (FreSCa cryo-SEM)[44,45]. For this technique, the water/oil interface is vitrified by a a propane jet

freezer and exposed by fracturing the frozen sample. Coating by a thin tungsten layer at a 30° angle with respect to the interface is used to make the sample conductive for SEM imaging. This process also allows measuring the protrusion height of features, if they cast a shadow after the tungsten coating. More details are given in Section 3.2.

The images in Fig. 1 show the appearance of the Big and Small microgels at a water-decane interface after fracture and oblique coating. By comparing the two images, it appears evident that the Big microgels have a pronounced core-shell morphology, while such feature is not clearly detected in the image of the Small particles, due to smaller material contrast. Nonetheless, it will appear clear later that the Small particles are also core-shell objects, even though the cross-linking gradients may be less pronounced than for the Big microgels. Furthermore, it can be seen that neither of the particle types casts any shadow. Therefore, an effective contact angle below 30° can be assumed and confirms the particle's hydrophilic character[42]. Finally, it is often not an easy task to accurately estimate the dimensions that core-shell particles take up at an interface from FreSCa images due to poor contrast coming from thin polymer layers, especially after short freeze-etching times, and to particle proximity. For these reasons, we estimate the particle sizes at the interface after deposition and drying and confirm the validity of these measurements by comparing these sizes with the ones that correspond to inter-
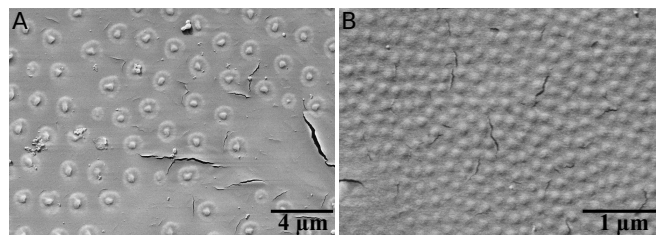

Fig. 1 FreSCa cryo-SEM images of the Big (**A**) and Small (**B**) microgels spread at the water/decane interface. The interface is shown after removing the oil and we observe the particles protruding from the water. Since the interface was coated with tungsten at an angle of 30° relative to the interface, and both microgels do not cast any shadow, their contact angle is below 30°, confirming their hydrophilic nature.

particle contacts at the point where the surface pressure starts increasing during a compression isotherm, as reported later (see Table 1).

The size and morphology of isolated microgels deposited onto a silicon wafer from a water/hexane interface can be seen in the AFM images of Fig. 2. Fig. 2A-B respectively show the height and phase images of a Big microgel after deposition and drying. The core-shell nature of this particle is particularly evident from the phase image, which clearly shows the extent of the spread shell, and which is difficult to visualize in the height image. Fig. 2C-D show the corresponding images for Small microgels. Fig. 2C illustrates that the particles have very irregular shapes, still presenting a core-shell structure, but in which the polymers are not evenly distributed. The dimensions of the particles can again be better visualized in the
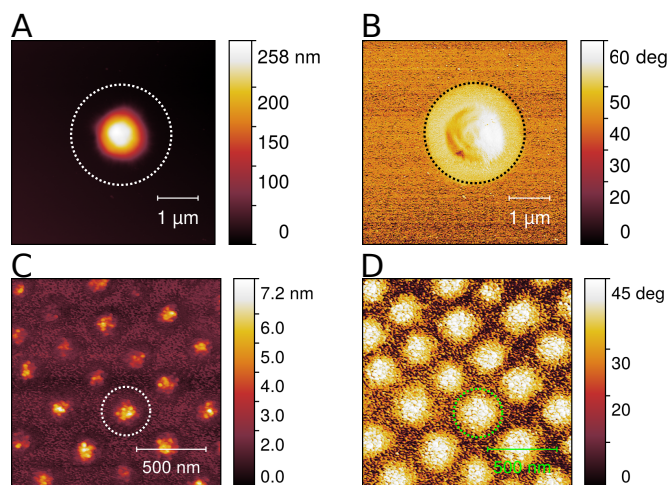
Fig. 2 AFM height and phase images of both Big **(A-B)** and Small **(C-D)** microgels after deposition on a silicon substrate from the water/hexane interface. The circles indicate the size of these microgels, including the shell, observed in the phase images. The lateral bars in (A-C) shows the height range from the minimum to the maximum height in the image.

Table 1 Size of microgels: diameters in bulk d_W (by DLS), after deposition on a silicon substrate from the water/hexane interface d_d (by AFM) and by the inter-particle contacts at low surface pressures d_i, when the surface pressure starts to increase in a compression curve (by AFM).

Microgel	d_W (nm)	d_d (nm)	d_i (nm)
Big	1454±278	2421±57	2297±40
Small	214±1	274±31	312±20

2.2 Two-dimensional phase behavior of microgel mono-layers upon compression

After discussing the properties of the individual microgels, we focus our attention on the ensemble structural behavior of microgel monolayers confined at a water-hexane interface. Monolayers of varying initial concentrations are prepared by spreading different amounts of microgels at an oil-water interface inside a Langmuir trough, whose barriers are then used to compress the monolayers to different levels of surface pressure Π. It is important to note that we do not have direct control of the number of microgels that adsorb at the water/hexane interface during spreading, because some of them can be lost into the aqueous sub-phase. For this reason, we determine the area per particle A_p after the deposition, by counting the number of particles per unit area in different AFM images of the silicon substrate corresponding to different values of the

phase image, which also highlights the non-uniform polymer distribution at these length scales. Deposited microgel sizes (d_d) were extracted from the phase images and are reported in Table 1. In the case of the Big microgels, the particles can also be visualized directly at the water-oil interface using a confocal microscope (see Fig. S1 in the Supplementary Information). Here, only the cores are visible, but the average distance between neighboring microgels in steric contact through their shells is $2.48 \pm 0.23\,\mu m$, very close to d_d. This also confirms the validity of the particle dimensions extracted ex-situ after deposition.

surface pressure at which that portion of the monolayer was deposited [14,26]. More details are given in Section 3.3.

The compression isotherm of the Big microgels at a water/hexane interface is shown in Fig. 3. Since it is not possible to obtain the full isotherm in one experiment because the compressible area of our Langmuir trough is too small, we carried out several different experiments with varying initial volumes of microgel dispersion spread at the water/hexane interface (indicated by the different colors). The combination of these is used to construct the full isotherm. The dashed lines in Fig. 3 define five different regions in the compression curve, where the corresponding structure of the monolayer is illustrated by the AFM images. It is clearly visible how the arrangement of the microgels changes during the compression. At the very beginning of the compression, in region I, the surface pressure increases very slowly when reducing A_p. In this region, the microgels are forming islands with empty spaces in between. The presence of these clusters implies the existence of attractive forces at the interface, which have also recently been observed and rationalized by Huang et al. [46] for similar microgels in terms of a balance between capillary attraction and steric repulsion between shells. The capillary interactions must be coming from small deformations of the interface generated by the wetting of the particle shells. This has also been recently highlighted for nanoparticles with hard cores and soft polymeric shells [21]. The latter colloids showed

a qualitatively identical compression curve to the one reported in Fig. 3, which is different from the ones of previously investigated microgels [14,26], indicating a subtle interplay between particle size, morphology and wetting. Moreover, we tried to elucidate if in our case the aggregation could be considered an artifact of the deposition. To this aim, we observed the Big microgels adsorbed at a water/hexadecane interface in a fluorescent confocal microscope, and verified that the same aggregation patterns that we observed after deposition on the substrate are already present. Additionally, we found that the average distance between Big microgels in those aggregates at the water/hexadecane interface was $(2480 \pm 230)\, nm$, in good agreement with the distances reported in Table 1 and with the average distance between Big microgels observed by optical microscopy once that they are deposited from the interface: $(2520 \pm 240)\, nm$ (see Fig. S1 in the Supplementary Information).

Upon further compression of the interface, the surface pressure starts to rise steeply, associated to the formation of an hexagonal crystalline phase where microgels interact sterically through their shells. In this region II, increasing the surface pressure causes a compression of the crystal, with fine tuning of the lattice constant. The onset of region II corresponds to the minimum distance between touching particles forming a uniform two-dimensional hexagonal packing and can therefore be used to estimate the size of the microgels

at the interface. This quantity is $(2297 \pm 40)\,nm$ and closely matches the diameter measured by AFM after deposition, as reported in Table 1. Thus, the effective diameter in which the Big microgels enter in steric contact is the one measured by AFM phase imaging.

The compression curve flattens again in region III. Here, upon further reducing A_p, islands of particles in closer contact start to form and grow. These new clusters consist of particles whose shells are no longer able to sustain the pressure and collapse into islands of an hexagonal, more closely-packed phase. This phase transition continues until all of the microgels are in the close-packed state, labeled as region IV, where a small window of compression causing a very steep surface pressure rise can be seen. However, soon after, the monolayer starts to buckle, as it can be observed in the AFM image corresponding to region V.

As already briefly mentioned, the Big microgels reproduce a behavior similar to the case of smaller P(Nipam-co-MAA) core-shell microgels studied in a previous work[26], with the same regions observed upon compression of the monolayer at the water/oil interface and with a transition between two hexagonal crystalline phases of different lattice constants. The main structural difference is observed at the lowest surface pressures in region I, where no fluid phase is observed and where clusters of particles with their shells in contact are obtained due to capillary forces, in analogy to what has
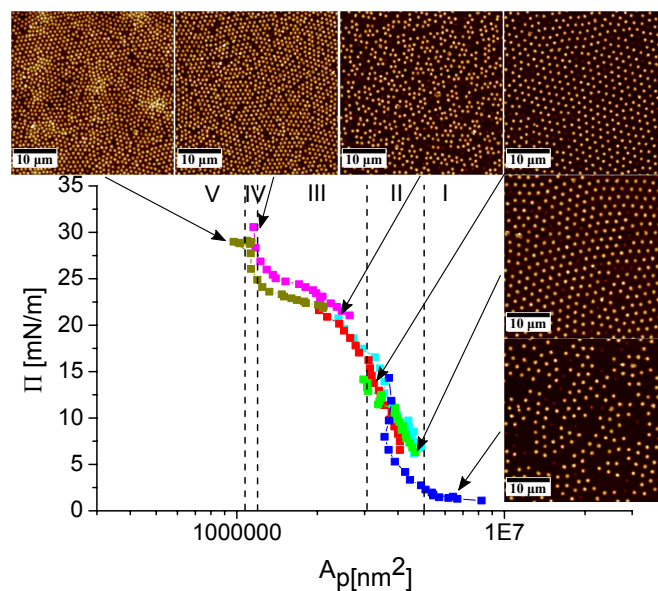

Fig. 3 Compression isotherm of the Big microgels, obtained from six individual measurements with varying spread microgel concentration indicated by the different colors of the curves (blue $70\,\mu L$ at 0.8 wt%, green for $65\,\mu L$, light blue for $120\,\mu L$, red for $60\,\mu L$, purple for $180\,\mu L$ and gold for $350\,\mu L$). The non-monotonic dependence of the surface pressure with the nominally injected particle number once more emphasizes the necessity to calculate A_p directly from the AFM images after deposition, since uncontrolled amounts of spread particles can be lost in the aqueous sub-phase. The dashed lines define the five different regimes of the phase diagram. Insets: AFM images taken on different substrates at different surface pressures.

been observed for other microgels and for hard core-soft shell nanoparticles[21]. Nevertheless, this behavior is not observed for the Small microgels. Figure 4 depicts the compression isotherm of the Small microgels. As for the other microgel type, several depositions with varying spread microgel

amounts (indicated by the different colors) were conducted and combined into a single isotherm. In contrast to the Big microgels and the particles described in our previous work[26], only three different regions corresponding to just as many phases can be identified here, as visualized by the AFM images. At the lowest compressions, in region I, the surface pressure increase is slow and the particles form a fluid, gas-like phase. Here, no aggregation is seen, and capillary interactions appear to be negligible. Upon reduction of the available area, a critical inter-particle distance is reached, where a two-dimensional crystal of particles in shell contact is formed. As soon as this region II starts, the surface pressure increases very steeply as the 2D crystal is compressed. The curves exhibit a plateau in region III, where a dense, disordered monolayer is formed and further compressed. This behavior is markedly different from the Big microgels, and the other core-shell systems we have previously investigated. No phase transition between two hexagonal crystalline phases is observed, but rather the system smoothly evolves into a continuously compressed dense liquid-like monolayer. The reason for this response may be ascribed to the heterogeneity of the structure of the Small particles, as visualized in Fig. 2C-D and as opposed to the clear architecture of the Big microgels seen in Fig. 2A-B, implying that the shells of the single particles can be continuously compressed rather than suddenly fail and collapse.

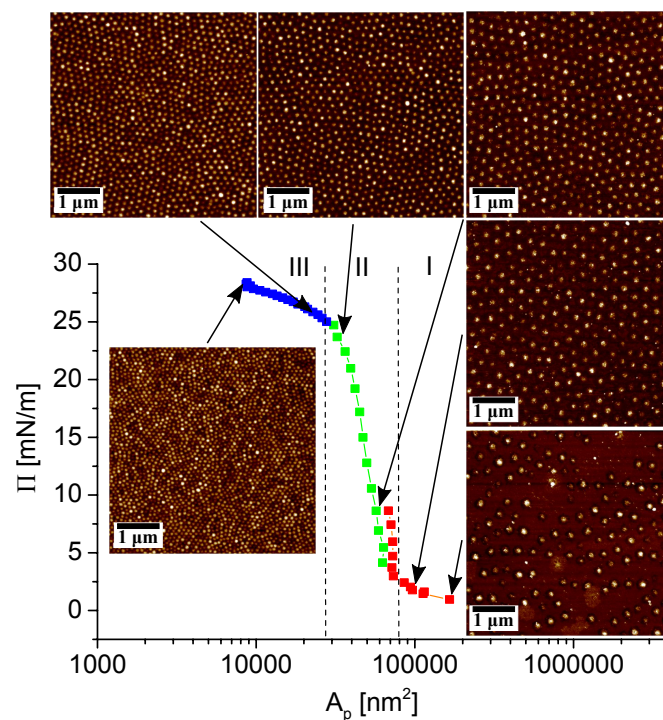The description of the compression behavior of the two

Fig. 4 Compression isotherm of the Small microgels, obtained from three individual measurements with varying microgel concentration indicated by the different colors of the curves (red for $15 \mu L$ at 0.5 wt%, green for $200 \mu L$ at 0.1 wt% and blue for $120 \mu L$ at 0.5 wt%). The dashed lines define the three different regimes of the phase diagram. Inset: AFM images taken on different substrates at different surface pressures.

microgel types can be further detailed by quantitatively investigating the average hexagonal order parameter $< \Psi_6 >$ and the average distance between neighboring particles as a function of A_p, extracted from the AFM images after locating the centers of each deposited microgel. The simultaneous analysis of these two quantities allows a more robust identification of the structural regimes described above. Fig. 5A

illustrates this approach for the Big microgels. Starting from region I, we observe that the order parameter increases steadily upon compression, but the inter-particle distance d stays constant. The combination of these two facts is connected to the creation of islands of particles having a hexagonal arrangement, driven by capillarity even at very low particle concentrations. The particles form 2D hexagonally packed clusters, where their separation is dictated by the shell thickness. By compressing the monolayer, the particle islands are brought together, causing a general increase of the hexagonal order without altering the inter-particle distance within the clusters. As mentioned above, this value of d shown in region I of Fig. 5A corresponds to the inter-particle separation directly measured at the interface from confocal images $(2480 \pm 230)\,nm$ and also to the inter-particle distance obtained from optical micrographs of Big particles deposited at low surface pressure from water-hexane interfaces, i.e. $(2520 \pm 240)\,nm$ (see Fig. S1). Region II is characterized instead by a constant and high value of Ψ_6 but a smoothly decreasing inter-particle distance. This corresponds to the fact that all the particle islands in region I have merged, leading to the creation of an hexagonal poly-crystalline monolayer, whose lattice constant is smoothly reduced upon compression, without distorting its structure. The onset of the solid-solid phase transition in region III is marked by a sudden drop of Ψ_6 and correspondingly by the appearance of

two nearest neighbor distances between the particles. These two values correspond to particles remaining in the non close-packed phase and particles belonging to the clusters of the new more closely packed phase. The value of the order parameter reaches a minimum when equal amounts of particles are in the two phases and starts growing again as more and more particles are in the second hexagonal phase, until a full close-packed monolayer is formed and Ψ_6 plateaus again at a high value in region IV. The completion of the phase transition is also marked by the re-merging of the two values of d into one single value. Region IV is very narrow and it is followed by monolayer buckling as detected from a loss of hexagonal order in region V.

The analysis of the data in Fig. 5B emphasizes the difference between Big and Small particles. In region I, the hexagonal order parameter grows, but the values of d correspondingly decrease. This confirms that the monolayer gets uniformly denser, as expected for repulsive particles in a gas-like phase. This is in contrast to the case of the Big particles, where compression only brings particle islands closer to each other. The transition into region II is marked by steep increase of Ψ_6 which then stays constant as the hexagonal crystal is compressed and the lattice spacing is correspondingly reduced. Another marked difference with the Big microgels is seen when moving into region III. Here, the transition be-

tween these two regions is not as sharp or as clear as for the Big particles and it can only be visualized by noting a continuous decrease of Ψ_6 until a plateau at a low level corresponding to a dense disordered liquid is found. Across all these transitions, no distinctive features can be seen for d, which remains single-valued and simply decreases smoothly and monotonically.

2.3 Etching

The degree of control in depositing microgel monolayers of tuneable structure affords their use as elements for nanolithography masks over large areas. We have in fact previously shown that microgels of an intermediate size between the Big and the Small particles can be effectively used as masks for the top-down chemical etching of arrays of vertically aligned silicon nanowires (VA-SiNWs)[14,29,30]. The process, that we termed soft nanoparticle lithography, required an essential step, where the thickness of the deposited microgels was increased by swelling them in photoresist to produce spots that would act as effective spacers between the underlying silicon substrate and a sputtered thin gold layer. The separation between the two materials inhibits a catalytic etching reaction, called metal-assisted chemical etching or MACE[14,29,30]. The reaction instead proceeds fast where there is contact between the silicon and the gold, leading to the chemical etching of the material around the microgels, which therefore determines

the position of VA-SiNWs. The diameter of the microgel core corresponds to the NW diameter, while the pitch of the NW array is determined by the surface pressure during deposition for area fractions corresponding to region II and the NW height is tuned by the etching time[14,29,30]. More details are given in Section 3.4.

The technical open question that remained after those studies was if the range of geometrical parameters of the produced VA-SiNWs could be further tuned by using microgels of significantly different sizes. Here we demonstrate that the process works successfully for the Big microgels but cannot be carried out for the Small ones.

Figure 6A shows the height cross-sections of Big and Small microgels before (solid curves) and after swelling (dashed curves) with the photoresist, confirming that the volume is increased after infiltration with the photoresist. Nevertheless, at this point it is possible to understand why we were not successful in obtaining VA-SiNWs with the Small microgels. Even after swelling their volume was insufficient to provide effective masking for MACE.

Conversely, the Big microgels could be successfully processed as etching masks for the fabrication of large-area arrays of VA-SiNWs with diameters in the micron range, as shown in Fig. 6B-C. We have also previously shown that the diameter of the NWs can be finely tuned by exposing the deposited
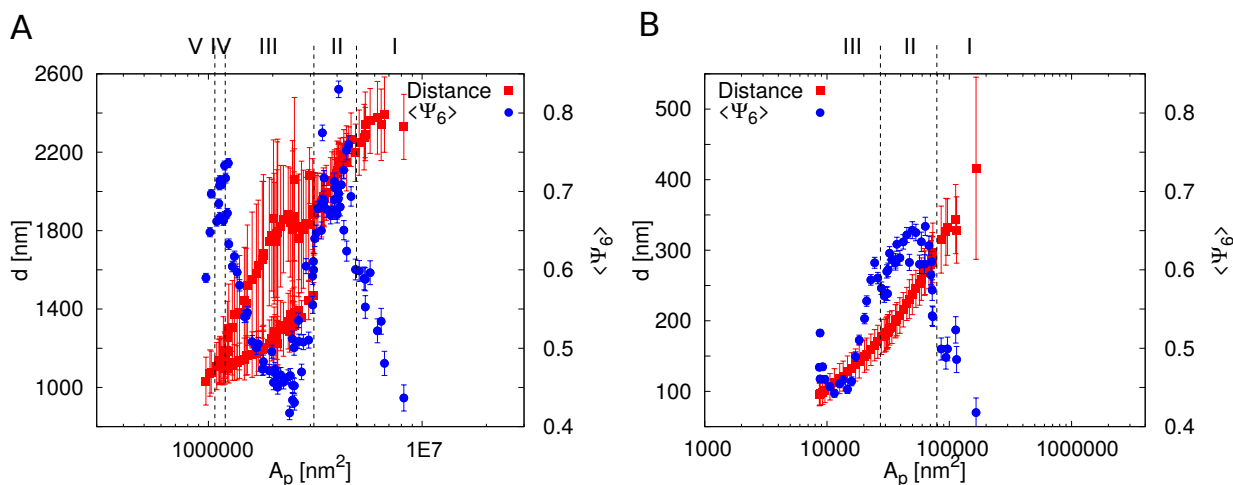
Fig. 5 Detailed analysis of the different microgel arrangements. $< \Psi_6 >$ module and average distance between neighboring particles d against the area per particle A_p for **(A)** the Big and **(B)** Small microgels, respectively.

microgels to an O_2 plasma for different times. Exposure to plasma leads to slow etching of the organic particles, and thus allows for finely tuning their dimensions before MACE, as shown in the inset to Fig. 6A. The height profiles measured by AFM also clearly show that the microgels acquire a more non-uniform shape after swelling. This makes it therefore difficult to adjust their diameters after swelling and the O_2 plasma treatment is thus applied before swelling. The plots in Fig. 6A finally show that the particles can still be swollen after plasma treatment and thus used for VA-SiNWs fabrication.

3   Experimental

3.0.1   Microgels The two types of microgels were synthesized in a similar way as described in previous works[27,42,47]: labeled as Big and Small microgels. While the Big micro-

gels were produced in two steps with further growth a pure pNipam shell onto a p(Nipam-co-MAA) core-shell microgel, the Small microgels are simple p(Nipam-co-MAA) core-shell particles. The microgels were labeled with a fluorescent dye: methacryloxyethylthiocarbamoyl rhodamine B (MRB, PolySciences). The Big(Small) microgels contain 0.0057 mol%(0.0165 mol%) of dye with reference to the monomers in the synthesis. Their bulk diameters were measured by dynamic light scattering (DLS, Zetasizer, Malvern UK) at $25\,^{\circ}C$ in milli-Q water. The Big microgels were further analyzed at the water/hexadecane interface (n-hexadecane $> 99\%$, Sigma-Aldrich, Germany) by fluorescence confocal microscopy (Visitron Spinning Disk, Yokogawa Confocal Scanner Unit CSU-W1-T2 with a Nikon Eclipse T1 microscope). After synthesis, all particles were stored in milli-Q water at $1\,wt\%$.
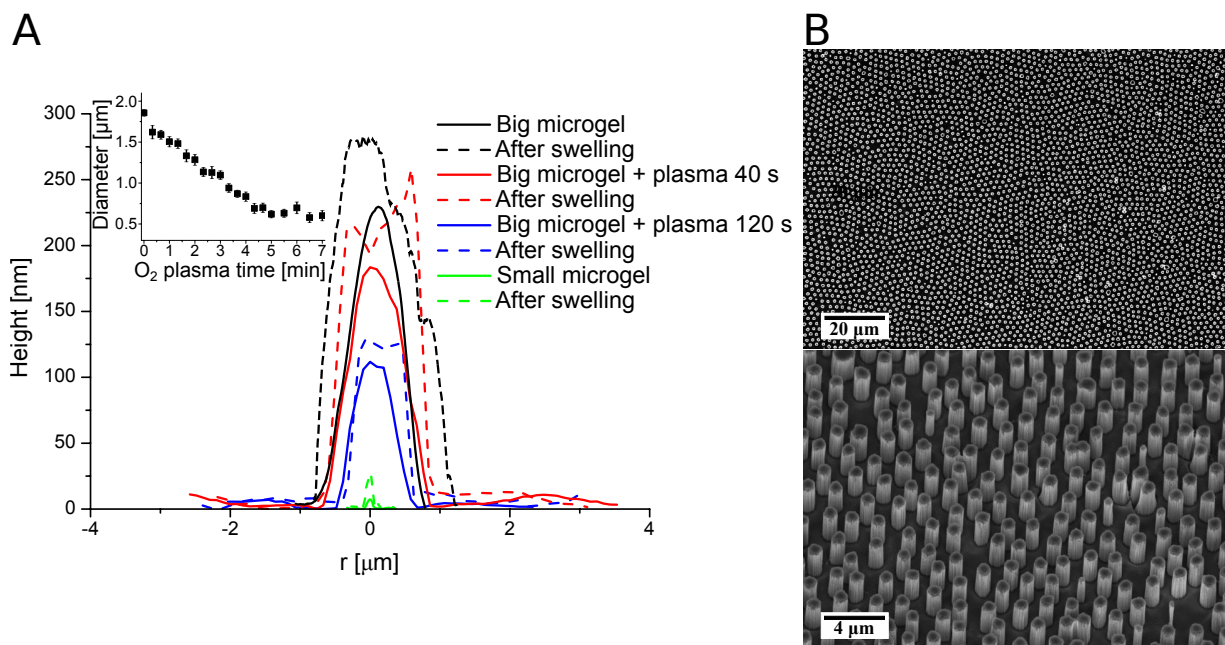
Fig. 6 A. Cross-sections of Big and Small microgels before (solid curves) and after (dashed curves) swelling with photoresist and the effect of 40 s and 120 s of O_2 plasma treatment on the Big microgels before and after swelling. The inset shows the width of the microgels upon different duration of the O_2 plasma treatment. **B**. Top and 30° tilted views of VA-SiNWs by SEM obtained after MACE of the Big microgels. The samples were etched for 20 min and the VA-SiNWs have a length of approximately $3\,\mu m$.

Prior to spreading they were diluted with isopropanol (IPA, Fisher Chemical, 99.97 %) and milliQ-water to $0.8\,wt\%$ with a 4:1 water dispersion:IPA ratio for the Big microgels and to $0.5\,wt\%$ with a 4:1:3 water dispersion:IPA:water ratio for the Small microgels.

3.1 Wafer preparation

Silicon wafers with a (100) orientation (from Siltronix or Siegert Wafer, p-type (boron-doped), $3 - 6\,\Gamma cm$) were cut into pieces of $1x2\,cm^2$ and ultrasonicated in toluene (Fluka Analytical, 99.7 %), isopropanol and milli-Q water for 15 min in each case. After drying under a N_2 stream, the wafers were treated in a Piranha solution ($3:1 H_2SO_4 : H_2O_2$) for 20 min, washed with milli-Q water and again dried with N_2. Then, they were put into an UV-ozone cleaner (UV/Ozone Procleaner Plus, Bioforce Nanosciences) for 10 min, and afterwards silanized with 3-amino-propyltriethoxysilanes (APTES; Sigma Aldrich, 99 %) for 2 hours using vapor deposition. Finally, the wafers were washed in toluene and milli-Q water for 10 min each and dried in N_2 prior to their use in the deposition protocol described below.

3.2 Freeze fracture shadow casting cryogenic scanning electronic microscopy

Freeze fracture shadow casting cryogenic scanning electron microscopy, abbreviated as FreSCa cryo-SEM, was performed by placing the microgel dispersion on a custom-made copper holder. Next, n-decane was added on top of the water dispersion to create a water/n-decane interface and a top copper cap sealed the copper holder. Afterwards, the sealed copper holder was vitrified using a liquid propane jet freezer (Bal-Tec/Leica JFD 030, Balzers/Vienna), mounted onto a double-fracture cryo-stage and transferred under inert gas in a cryo-high vacuum airlock ($< 5 \cdot 10^{-7}$ mbar, Bal-Tec/Leica VCT010) to a precooled freeze-fracture machine at -140 °C (Bal-Tec/Leica BAF060 device). The fractured interface was freeze-dried at -110 °C for 1 min. The two halves of the sample were coated at a temperature of -120 °C by unidirectional tungsten deposition forming 30° with the sample to a thickness of 2 nm, followed by an additional 2 nm at a varying angle between 90° and 30°. The tungsten-coated samples were then transferred to a precooled (-120 °C) cryo-SEM (Zeiss Gemini 1530, Oberkochen) under same high vacuum conditions and observed with a secondary electron detector.

3.3 Microgel deposition using the Langmuir trough

The compression curves were produced using a Langmuir trough (KSV 5000) equipped for water-oil interfaces and for deposition placed in a hood. The trough was previously cleaned by rinsing it several times with ethanol (Fluka Analytical, 99.8 %) and milliQ-water. Once that the substrate was fixed on the dipping arm with a plastic screw, it was placed inside the trough forming 30° angle with the interface. The surface pressure was measured by a Wilhelmy plate ($2x1\,cm$) made out of roughened platinum. The trough was filled with water until the barrier level, the Wilhelmy plate was immersed by one third of its height, and the substrate was placed just below the water/air interface. The next step consisted in compressing the barriers and removing possible contaminations at the interface using with a pipette tip attached to a vacuum pump. This operation was repeated until the surface pressure never increased above than 0.2 mN/m. Next, 100 ml of hexane (Sigma Aldrich, 99 %) were poured in the trough and finally the desired amount of microgel suspension was deposited with a Hamilton microsyringe of $250\,\mu l$. The trough allowed for simultaneously compressing or expanding the barriers while lifting the Si substrate through the interface, which permitted to create gradients of suraface coverage on the substrates with different densities of microgels at different positions on the sample. After 10 min of stabilization, the compression and the dipping started at the same time with a barrier speed of 2.3 mm/min and a dipping upward speed of 0.3 mm/min to ensure that at the maximum compression (after 70 mm of barrier movement) the substrate crossed the water/hexane interface.

Then, the substrate continued rising until it was completely in air and was recovered.

3.4 Fabrication of VA-SiNWs

First, the deposited microgel arrays were swollen using the photoresist AZ1518 (Clariant GmbH, Germany). The photoresist was pipetted onto the substrates and allowed to stand for 30 min. Then the substrates with the photoresist were heated on a heating plate for 1 min at $100\,^{\circ}C$. Later, the photoresist was washed off with acetone (Sigma Aldrich, 99 %). The substrates were washed in ethanol and dried in air under a steep angle. Following the swelling, the substrates were put into an oxygen plasma cleaner (PDC-32G, Harrick Scientific Corporation) in order to reduce the diameter of the microgels. The Big microgels were first plasma treated and then swollen. Before the metal-assisted chemical etching (MACE), a 15 nm-thick gold layer was sputtered (CCU-010, safematic GmbH) onto the substrates coated with the swollen Big microgels at a current of 30 mA, a pressure of $3 \cdot 10^{-2}$ mbar and a working distance of 70 mm. The MACE was carried out in a Teflon beaker. The etching solution, with a 20 ml total volume, had the following composition: 4 ml HF (Sigma Aldrich, 48 %), 10 ml ethanol, 2 ml hydrogen peroxide (Merck, 30 %) and 4 ml milli-Q water. In order to remove the gold layer and microgels after MACE, the substrates were exposed to a I_2/KI (Sigma Aldrich, ¿99 %) solution (1:4:40, $I_2/KI/H_2O$) for 15 min to remove the gold layer. They were subsequently washed in milli-Q water and acetone and dried in N_2. The microgels were finally removed by oxygen plasma (5 min).

3.5 Surface characterization

Directly after the deposition, the microgel arrays were analyzed with an AFM (Bruker Icon Dimension) in tapping mode using micro cantilevers (Olympus, typical resonance frequency: 300 kHz, typical spring constant: 26 N/m). Starting at the upper edge (the one that came out of the hexane first), an image was taken every 1 mm. This procedure allowed to monitor the development of the compression of the microgel monolayer. Depending on the microgel type, the scan size varied between 5x5 and 40x40 μm^2 at 512x512 pixel^2. The AFM images were flattened and a grey scale was added, so that they could be analyzed with a custom-written particle tracking software, as in previous works[14,26]. Using this software, the area per particle A_p, the nearest-neighbor distances and the hexagonal order parameter Ψ_6 were extracted from the AFM images. The silicon wafers with the VA-SiNWs were analyzed using a LEO 1530 SEM (Zeiss; acceleration voltage 5 kV). The secondary electron or in-lens detector was used for the SEM analysis.

4 Conclusions

In this work we studied the compression behavior of two differently sized microgels confined at a water-oil interface. Single-particle investigations revealed that both particles have a core-shell morphology, with interfacial dimensions that are significantly larger than their bulk sizes. Albeit apparently similar in morphology, the two particles show markedly different response under compression. In particular, the Big microgels display evidence of attractive capillary forces, which drive the formation of two-dimensional clusters at low interface coverage. Upon further compression, these islands, which have local hexagonal crystalline order of particles contacting via their shells, are merged into an hexagonal crystalline monolayer, which further undergoes a phase transition to a second hexagonal lattice with particles in core contacts. Conversely, the Small particles do not appear to interact via capillarity and form a gas-like phase at low surface coverage. Upon reaching a critical area fraction corresponding to particles in steric contacts through their shells, also here an hexagonally packed crystalline monolayer is formed, but no solid-solid phase transition between two crystalline lattices is observed and the monolayer gets simply smoothly compressed into a dense disordered structure. We have furthermore demonstrated that particle size is a crucial parameter to turn the microgels into effective masks for metal-assisted chemical etching of silicon nanowires. A sufficient thickness of the microgels after swelling is required to provide effective masking. In the case of the Big particles, they could be successfully used for soft particle templating to fabricate tuneable arrays of vertically aligned silicon nanowires. In this case, the microstructure of the nanowire array directly reflects the microstructure of the microgel monolayer at the interface, emphasizing the need to be able to understand and harness the behavior of the particles to produce controlled nanopatterns.

Our findings therefore prompt further investigations on the detailed role played by particle architecture, morphology, mechanical properties and size on the formation and compression of monolayers at fluid interfaces with the promise to extend their applicability as robust and versatile nanopatterning elements.

References

1 J. Zhang, Y. Li, X. Zhang and B. Yang, *Adv. Mater.*, 2010, **22**, 4249–4269.

2 J. B. Thorne, G. J. Vine and M. J. Snowden, *Colloid Polym. Sci.*, 2011, **289**, 625–646.

3 P. J. Yunker, K. Chen, M. D. Gratale, M. A. Lohr, T. Still and A. G. Yodh, *Rep. Prog. Phys.*, 2014, **77**, 056601.

4 B. R. Saunders and B. Vincent, *Adv. Colloid Interface Sci.*, 1999, **80**, 1–25.

5 J. Kim, S. Nayak and L. A. Lyon, *J. Am. Chem. Soc.*, 2005, **127**, 9588–9592.

6 G. R. Hendrickson, M. H. Smith, A. B. South and L. A. Lyon, *Adv. Funct. Mater.*, 2010, **20**, 1697–1712.

7 L. Hu and M. J. Serpe, *ACS Appl. Mater. Interfaces*, 2013, **5**, 11977–11983.

8 S. Tsuji and H. Kawaguchi, *Langmuir*, 2005, **21**, 8439–8442.

9 Y. Xia, X. He, M. Cao, C. Chen, H. Xu, F. Pan and J. R. Lu, *Biomacro-molecules*, 2013, **14**, 3615–3625.

10 T. Still, P. J. Yunker, K. Hanson, Z. S. Davidson, M. A. Lohr, K. B. Aptowicz and A. G. Yodh, *Adv. Mater. Interf.*, 2015, **2**, 10.1002/admi.201570078.

11 A. Burmistrova and R. von Klitzing, *J. Mater. Chem.*, 2010, **20**, 3502–3507.

12 K. Horigome and D. Suzuki, *Langmuir*, 2012, **28**, 12962–12970.

13 J. Peng, D. Zhao, X. Tang, F. Tong, L. Guan, Y. Wang, M. Zhang and T. Cao, *Langmuir*, 2013, **29**, 11809–11814.

14 M. Rey, R. Elnathan, R. Ditcovski, K. Geisel, M. Zanini, M.-A. Fernandez-Rodriguez, V. V. Naik, A. Frutiger, W. Richtering, T. Ellenbogen, N. H. Voelcker and L. Isa, *Nano Lett.*, 2016, **16**, 157–163.

15 M. Karg and T. Hellweg, *Curr. Opin. Colloid Interface Sci.*, 2009, **14**, 438–450.

16 N. Vogel, C. Fernández-López, J. Pérez-Juste, L. M. Liz-Marzán, K. Landfester and C. K. Weiss, *Langmuir*, 2012, **28**, 8985–8993.

17 T. Honold, K. Volk, A. Rauh, J. P. S. Fitzgerald and M. Karg, *J. Mater. Chem. C*, 2015, **3**, 11449–11457.

18 K. Volk, J. P. S. Fitzgerald, M. Retsch and M. Karg, *Adv. Mater.*, 2015, **27**, 7332–7337.

19 K. Geisel, A. A. Rudov, I. I. Potemkin and W. Richtering, *Langmuir*, 2015, **31**, 13145–13154.

20 K. Özlem Nazli, C. W. Pester, A. Konradi, A. Böker and P. vanRijn, *Chem. Eur. J.*, 2013, **19**, 5586–5594.

21 A. Rauh, M. Rey, L. Barbera, M. Zanini, M. Karg and L. Isa, *Soft Matter*, 2016, 10.1039/C6SM01020B.

22 A. Fernández-Barbero, A. Fernández-Nieves, I. Grillo and E. López-Cabarcos, *Phys. Rev. E*, 2002, **66**, 051803.

23 M. Stieger, W. Richtering, J. S. Pedersen and P. Lindner, *The Journal of Chemical Physics*, 2004, **120**, 6197–6206.

24 J. Zhang and R. Pelton, *Langmuir*, 1999, **15**, 8032–8036.

25 K. Geisel, L. Isa and W. Richtering, *Angew. Chem. Int. Ed.*, 2014, **53**, 4905–4909.

26 M. Rey, M. A. Fernandez-Rodriguez, M. Steinacher, L. Scheidegger, K. Geisel, W. Richtering, T. M. Squires and L. Isa, *Soft Matter*, 2016, **12**, 3545–3557.

27 K. Geisel, W. Richtering and L. Isa, *Soft Matter*, 2014, **10**, 7968–7976.

28 F. Pinaud, K. Geisel, P. Masse, B. Catargi, L. Isa, W. Richtering, V. Ravaine and V. Schmitt, *Soft Matter*, 2014, **10**, 6963–6974.

29 R. Elnathan, L. Isa, D. Brodoceanu, A. Nelson, F. J. Harding, B. Delalat, T. Kraus and N. H. Voelcker, *ACS Appl. Mater. Interfaces*, 2015, **7**, 23717–23724.

30 R. Elnathan, B. Delalat, D. Brodoceanu, H. Alhmoud, F. J. Harding, K. Buehler, A. Nelson, L. Isa, T. Kraus and N. H. Voelcker, *Adv. Funct. Mater.*, 2015, **25**, 7215–7225.

31 K. Peng, J. Jie, W. Zhang and S.-T. Lee, *Appl. Phys. Lett.*, 2008, **93**, 033105.

32 E. Mills, J. Cannarella, Q. Zhang, S. Bhadra, C. B. Arnold and S. Y. Chou,

J. Vac. Sci. Technol. B, 2014, **32**, 06FG10.

33 R. Huang, X. Fan, W. Shen and J. Zhu, *Appl. Phys. Lett.*, 2009, **95**, 133119.

34 A. Vlad, A. L. M. Reddy, A. Ajayan, N. Singh, J.-F. Gohy, S. Melinte and P. M. Ajayan, *Proc. Natl. Acad. Sci. USA*, 2012, **109**, 15168–15173.

35 B.-R. Huang, Y.-K. Yang, T.-C. Lin and W.-L. Yang, *Sol. Energ. Mat. Sol. Cells*, 2012, **98**, 357–362.

36 H. E. Jeong, I. Kim, P. Karam, H.-J. Choi and P. Yang, *Nano Lett.*, 2013, **13**, 2864–2869.

37 Y. J. Hung, S. L. Lee, B. J. Thibeault and L. A. Coldren, *IEEE J. Sel. Top. Quantum Electron.*, 2011, **17**, 869–877.

38 J. Goldberger, A. I. Hochbaum, R. Fan and P. Yang, *Nano Lett.*, 2006, **6**, 973–977.

39 K. Peng, M. Zhang, A. Lu, N.-B. Wong, R. Zhang and S.-T. Lee, *Appl. Phys. Lett.*, 2007, **90**, 163123.

40 Z. Huang, H. Fang and J. Zhu, *Adv. Mater.*, 2007, **19**, 744–748.

41 T. Kawano, Y. Kato, M. Futagawa, H. Takao, K. Sawada and M. Ishida, *Sensor Actuat. A-Phys.*, 2002, **97-98**, 709–715.

42 K. Geisel, L. Isa and W. Richtering, *Langmuir*, 2012, **28**, 15770–15776.

43 K. Geisel, K. Henzler, P. Guttmann and W. Richtering, *Langmuir*, 2015, **31**, 83–89.

44 L. Isa, F. Lucas, R. Wepf and E. Reimhult, *Nat. Commun.*, 2011, **2**, 10.1038/ncomms1441.

45 L. Isa, *CHIMIA*, 2013, **67**, 231–235.

46 S. Huang, K. Gawlitza, R. von Klitzing, L. Gilson, J. Nowak, S. Odenbach, W. Steffen and G. K. Auernhammer, *Langmuir*, 2016, **32**, 712–722.

47 S. Schmidt, T. Liu, S. Rütten, K.-H. Phan, M. Mller and W. Richtering, *Langmuir*, 2011, **27**, 9801–9806.